Computer Methods in Applied Mechanics and Engineering 199 (2010) 1949–1962

Contents lists available at ScienceDirect

Computer Methods in Applied Mechanics and Engineering

journal homepage: www.elsevier.com/locate/cma

A Hermite cubic collocation scheme for plane strain hydraulic fractures

A. Peirce

Department of Mathematics, University of British Columbia, Vancouver, British Columbia, Canada V6T 1Z2

ARTICLE INFO

Article history:
Received 14 October 2009
Received in revised form 8 February 2010
Accepted 13 February 2010
Available online 4 March 2010

Keywords:
Hydraulic fractures
Integro-partial differential equations
Hermite cubic interpolation
Collocation methods

ABSTRACT

We describe a novel cubic Hermite collocation scheme for the solution of the coupled integro-partial differential equations governing the propagation of a hydraulic fracture in a state of plane strain. Special blended cubic Hermite-power–law basis functions, with arbitrary index $0<\alpha<1$, are developed to treat the singular behavior of the solution that typically occurs at the tips of a hydraulic fracture. The implementation of blended infinite elements to model semi-infinite crack problems is also described. Explicit formulae for the integrated kernels associated with the cubic Hermite and blended basis functions are provided. The cubic Hermite collocation algorithm is used to solve a number of different test problems with two distinct propagation regimes and the results are shown to converge to published similarity and asymptotic solutions. The convergence rate of the cubic Hermite scheme is determined by the order of accuracy of the tip asymptotic expansion as well as the $O(h^4)$ error due to the Hermite cubic interpolation. The errors due to these two approximations need to be matched in order to achieve optimal convergence. Backward Euler time-stepping yields a robust algorithm that, along with geometric increments in the time-step, can be used to explore the transition between propagation regimes over many orders of magnitude in time.

© 2010 Elsevier B.V. All rights reserved.

1. Introduction

Hydraulic fractures (HF) are a class of brittle fractures that propagate in pre-stressed solid media due to the injection of a viscous fluid. These fractures occur naturally when pressurized magma from deep underground chambers form vertical intrusions driven by buoyancy forces, which can in turn form geological structures such as dykes and sills [23,32–34]. In the oil and gas industry, HF are deliberately created in reservoirs to enhance the recovery of hydrocarbons by the creation of permeable pathways [15]. The application of HF in geotechnical engineering is growing. For example, in the mining industry they have recently been used to weaken the rock and enhance the so-called block-caving process [16,35]. Similarly, the extraction of geothermal energy requires the creation of new fractures to increase the existing fracture networks. Hydraulic fractures have also been used for waste disposal [2,3] and are likely to play a key role in the gravitational trapping of CO_2 in deep, low permeability, ocean sediments. The propagation of hydraulic fractures into undesirable locations can have severe safety consequences in the mining industry and can cause considerable loss of hydrocarbons and environmental damage in the oil industry. Likewise, the perforation of the caprock by HF can reverse the costly capture process involved in CO_2 sequestration. It is therefore of considerable importance to have accurate models in order to be able to predict the advance of HF to achieve an effective design of the engineering parameters in the injection process.

Mathematical models of HF involve a degenerate system of hypersingular integro-partial differential equations defined on a domain with a moving boundary. This class of problem has been shown to exhibit a multi-scale structure [13] in which the fracture can propagate in a number of different modes each determined by the dominant physical process active at the tip of the fracture. A number of studies on the propagation of HF in the special case of plane strain have clearly established the pivotal role of the asymptotic behavior of the solution in the vicinity of the fracture tip [6,12,13,18,25,33]. The tip behavior of HF propagating in a state of plane strain is also important for the analysis of planar HF in 3D elastic media. Indeed, in the vicinity of the perimeter of such a planar HF, the governing equations can be shown [30] to reduce to those of an HF propagating in a state of plane strain — provided the boundary of the fracture is smooth. In that paper the plane strain asymptotic solutions were combined with a level set algorithm to locate the free boundary for the propagating planar HF, which achieved remarkably accurate results with relatively modest computational resources. To proceed to more complex situations (such as material interfaces or discontinuities in the ambient geological stress field) there is a need to develop efficient algorithms to solve these more complex 1D plane strain problems. The objective of this paper is to develop a robust framework to solve this class of problems.

In order to treat the free boundary for such problems, Detournay et al. [14] introduced a time-dependent scaled coordinate system in

E-mail address: peirce@math.ubc.ca.

0045-7825/$ – see front matter © 2010 Elsevier B.V. All rights reserved.
doi:10.1016/j.cma.2010.02.009

which location of the free boundary is reduced to determining the fracture length as a function of time — for which there is an additional equation. Termed a moving-mesh algorithm this formulation introduces an additional convective term that is not present in the original PDE. Following the methodology introduced by Spence and Sharp [33] the integral operator is approximated by an expansion in basis functions comprising linear combinations of special solutions. The PDE is typically discretized with finite differences with upwinding for the convective term. For more complex problems identifying the appropriate basis functions is not a simple matter.

In this paper our objective is to develop an accurate and robust approach that relies on basis functions that are not tied to any one problem. It is also desirable to achieve compatible spatial discretizations for the integral equation and the system of PDE. It has long been recognized that to enable element-edge collocation for a mesh based discretization of the crack integral equation, C^1 continuity is a minimum requirement. Lower order continuity approximations are restricted to collocation away from element edges, while a Galerkin approach, which involves an additional integration of the kernel functions, is also used to regularize the singular fields at element edges. Natural C^1 or higher continuity, piecewise polynomial interpolants are either from the Hermite family or the class of B-splines (see [11]). On the other hand cubic Hermite collocation methods [7,21] are well established as robust techniques for solving two-point boundary value problems. Thus it is natural to consider a cubic Hermite approximation scheme for solving the coupled integro-partial differential equations governing the propagation of a plane strain HF. Cubic Hermite approximations to boundary element equations are not new either. Initially introduced by Watson [36] and developed further by a number of authors [26–28] they have not been widely adopted (see [19]) due to the additional degrees of freedom introduced by the derivatives (which increase with the number of dimensions). For crack problems this additional complexity may not be justified due to the singular nature of the solution at the tip in which the derivative of the crack aperture is infinite. Thus standard cubic Hermite interpolation cannot be used for the tip — indeed some form of tip element will have to be implemented. For the HF problem the nodal derivatives are not inconvenient additional degrees of freedom, but form an integral part of the algorithm in the approximation of the convective derivative.

The algorithm proposed in this paper makes use of a cubic Hermite scheme for the integral equation as well as to achieve the spatial discretization of the PDE. It is desirable that the algorithm have the flexibility to incorporate some form of tip element in order that the singular tip behavior, which can be established by local asymptotic analysis, can be incorporated directly. For HF the crack opening does not necessarily have the square root tip asymptotic behavior found in linear elastic fracture mechanics for toughness dominated fracture propagation. To cater for this, an arbitrary power–law tip asymptote has been incorporated into the formulation. The capacity to incorporate an arbitrary tip asymptote will make it possible to treat problems in which there is a transition from one propagation regime to another.

In Section 2, we state the governing equations for the propagation of a plane strain HF, introduce the scaling and non-dimensionalization of these equations, and establish the tip asymptotic behavior for the two propagation regimes that are considered in this paper. In Section 3, we describe the cubic Hermite basis functions, blended tip basis functions, integrals of these basis functions under the action of the hypersingular integral operator to yield the so-called 'influence functions'. The final subsection describes the coupled approximation scheme for the integral equation, the system of PDE, the volume balance constraint, and the boundary conditions. In Section 4, we present results of three numerical experiments. The first experiment considers the propagation of a plane strain HF in an elastic medium with zero toughness and compares the results to a similarity solution. The second experiment considers the propagation of a plane strain HF in the large toughness limit and compares the solution to an asymptotic solution. The last experiment considers a steady semi-infinite buoyancy driven crack in the large toughness limit and compares the results to those published in the literature. In Section 5, we make some concluding remarks. In Appendix A, the Mellin transform is used to determine the asymptotic behavior of the pressure in the vicinity of the fracture tips due to the action of the hypersingular integral operator for a finite fracture when acting on a fracture aperture field that has a given power–law behavior. These results are required to establish the appropriate tip asymptotic behavior that is used in the construction of the algorithm.

2. Problem formulation

2.1. Plane strain hydraulic fracture model

We consider a growing fracture that occupies the expanding interval $(-\ell(t),\ \ell(t))$ and which is forced to propagate in an impermeable elastic medium by the injection of a Newtonian fluid. The fluid is injected from a source that is located at the point $x=0$ at the volumetric rate Q_0 per unit length in the out-of-plane direction. A solution to this free boundary problem involves determining the evolving fracture length $\ell(t)$, the unknown fracture opening $w(x,\ t)$, and the net pressure $p(x,\ t)=p_f(x,\ t)-\sigma_c$. Here $p_f(x,\ t)$ is the fluid pressure and σ_c is the ambient geological confining stress, which is assumed to be known. The solution depends upon Q_0 and three material parameters for which it is convenient to introduce the following notation (after [13])

$$\mu' = 12\mu,\ E' = \frac{E}{1-\nu^2},\ K' = 4\left(\frac{2}{\pi}\right)^{1/2} K_{Ic}. \tag{2.1}$$

Here μ is the dynamic viscosity of the fluid, E and ν are the Young's modulus and Poisson's ratio of the elastic medium respectively, and K_{Ic} is the material toughness.

2.1.1. Elasticity equation

The crack opening w, which represents the elastic response of the solid medium to the net pressure p imposed on the fracture surfaces, is governed (see [20,24]) by the following integral equation

$$p(x,t) = -\frac{E'}{4\pi} \text{⨍}\!\!\!\!\!\!-_{-\ell}^{\ell} \frac{w(x',t)}{(x'-x)^2}\,dx' = -\frac{E'}{4\pi} \text{⨍}\!\!\!\!\!\!-_{-\ell}^{\ell} \frac{\partial w}{\partial x'}\frac{1}{x'-x}\,dx'. \tag{2.2}$$

Here $\text{⨍}\!\!\!\!\!\!-_{-\ell}^{\ell}$ represents a hypersingular integral which has to be interpreted in a Hadamard sense, while the symbol $\text{⨍}\!\!\!-_{-\ell}^{\ell}$ is used to denote a Cauchy principal value integral [24]. The equivalence of the above two forms of the integral equation can be established by integration by parts and recognizing that the fracture width w vanishes at the tips $\pm\ell$.

2.1.2. The Reynolds lubrication equation

2.1.2.1. Poiseuille's Law. The flux q of the viscous fluid within the fracture is assumed to be related to the pressure gradient and the fracture aperture according to Poiseuille's Law

$$q = -\frac{w^3}{\mu'}\frac{\partial p}{\partial x}. \tag{2.3}$$

2.1.2.2. Conservation law. The volume of fluid within the fracture is accounted for by the following conservation law

$$\frac{\partial w}{\partial t} + \frac{\partial q}{\partial x} = Q_0\delta(x). \tag{2.4}$$

We observe that by eliminating the flux q between Eqs. (2.3) and (2.4) we obtain the Reynolds lubrication equation [8]

$$\frac{\partial w}{\partial t} = \frac{1}{\mu'}\frac{\partial}{\partial x}\left(w^3\frac{\partial p}{\partial x}\right) + Q_0\delta(x). \tag{2.5}$$

2.1.3. Boundary conditions and the global volume balance condition

As mentioned above, the aperture vanishes at the fracture tips while there is also assumed to be zero flux at these points. These conditions can be expressed in the form

$$w(\pm\ell, t) = 0 \text{ and } q(\pm\ell, t) = 0. \tag{2.6}$$

Assuming symmetry of the left and right wings of the crack it can be shown that the source term can be replaced by the following equivalent flux boundary condition

$$q(0, t) = Q_0/2. \tag{2.7}$$

Integrating Eq. (2.4) over the interval $(-\ell(t), \ell(t))$ and using the boundary conditions (2.6) we obtain the following global volume balance condition

$$\int_{-\ell}^{\ell} w dx = Q_0 t. \tag{2.8}$$

2.1.4. Propagation condition

If the fracture half-length $\ell(t)$ was known, then Eqs. (2.2)–(2.6) are sufficient to determine the unknown width and pressure fields $w(x, t)$ and $p(x, t)$. However, in order to locate the free boundary $\ell(t)$ we require additional conditions at the fracture tips. In the case that the elastic material has a non-zero toughness, the mode I stress intensity factor K_I is assumed to be in limit equilibrium with the fracture toughness according to linear elastic fracture mechanics. This condition can be conveniently expressed [31] by the following asymptotic relation, which for the right tip, assumes the form

$$w \overset{x\to\ell^-}{\sim} \frac{K'}{E'}\sqrt{\ell - x}. \tag{2.9}$$

2.2. Scaling

In order to reduce the governing equations to dimensionless form we introduce the following scaled variables

$$x = \ell(t)\xi,\ \ell(t) = \ell_*\gamma(\tau),\ t = t_*\tau,\ w = w_*\Omega(\xi,\tau), \tag{2.10}$$
$$p = p_*\Pi(\xi,\tau),\ q = q_*\Psi(\xi,\tau).$$

We choose $p_* = E'\frac{w_*}{\ell_*}$, $q_* = \frac{w_*^3 p_*}{\mu'\ell_*}$, and identify the following dimensionless groups

$$\mathcal{G}_m = \frac{\mu'\ell_*^3}{w_*^3 E' t_*},\ \mathcal{G}_v = \frac{Q_0 t_*}{\ell_* w_*}, \text{ and } \mathcal{G}_k = \frac{K'\ell_*^{1/2}}{E' w_*}. \tag{2.11}$$

In terms of these scalings the elasticity Eq. (2.2) is reduced to the following dimensionless form

$$\Pi = -\frac{1}{4\pi\gamma}\fint_{-1}^{1}\frac{\Omega}{(\xi'-\xi)^2}d\xi' = -\frac{1}{4\pi\gamma}\fint_{-1}^{1}\frac{\partial\Omega}{\partial\xi'}\frac{1}{\xi'-\xi}d\xi' \tag{2.12}$$

while Poiseuille's Law (Eq. (2.3)) can be expressed as

$$\Psi = -\frac{\Omega^3}{\gamma}\frac{\partial\Pi}{\partial\xi}. \tag{2.13}$$

Finally, the conservation law (Eq. (2.4)) is reduced to the following dimensionless form

$$\gamma\frac{\partial\Omega}{\partial\tau} - \dot{\gamma}\xi\frac{\partial\Omega}{\partial\xi} + \mathcal{G}_m^{-1}\frac{\partial\Psi}{\partial\xi} = \mathcal{G}_v\delta(\xi). \tag{2.14}$$

We observe that due to the time dependence of the scaled coordinate $x = \ell(t)\xi$ an additional convective term appears in the scaled conservation law.

The corresponding scaled boundary conditions are given by

$$\Omega(\pm1, \tau) = 0,\ \Psi(\pm1, \tau) = 0, \tag{2.15}$$

while the global volume balance condition assumes the form

$$\gamma\int_{-1}^{1}\Omega d\xi = \mathcal{G}_v\tau. \tag{2.16}$$

The propagation condition, assuming non-zero toughness, is reduced to the form

$$\Omega \overset{\xi\to1^-}{\sim} \mathcal{G}_k\gamma^{1/2}\sqrt{1-\xi}. \tag{2.17}$$

The inlet flux condition (Eq. (2.7)), which is an alternative to the δ function source term in Eq. (2.14) and is also useful for an implementation in which symmetry is exploited, can be expressed in the form

$$\Psi(0, \tau) = \frac{1}{2}\mathcal{G}_v\mathcal{G}_m.$$

Viscosity scaling: $\mathcal{G}_m = \mathcal{G}_v = 1$.

This constraint allows one to identify the power–law relationship between the characteristic length and width and the characteristic time scale.

$$\ell_* = \left(\frac{E'Q_0^3}{\mu'}\right)^{1/6} t_*^{2/3},\ w_* = \left(\frac{Q_0^3\mu'}{E'}\right)^{1/6} t_*^{1/3}. \tag{2.18}$$

In this case we consider $\mathcal{G}_k = K'\left(\frac{1}{E'^3\mu' Q_0}\right)^{1/4}$ as a parameter.

Toughness scaling: $\mathcal{G}_k = \mathcal{G}_v = 1$.

As above, this constraint allows one to identify the power–law relationship between the characteristic length and width and the characteristic time scale.

$$\ell_* = \left(\frac{E'Q_0}{K'}\right)^{2/3} t_*^{2/3},\ w_* = \left(\frac{Q_0^{1/2}K'}{E'}\right)^{2/3} t_*^{1/3}. \tag{2.19}$$

In this case we consider $\mathcal{G}_m = \mu'\left(\frac{E'^3 Q_0}{K'^4}\right)^{1/4}$ as a parameter.

2.3. Tip asymptotics

In order to derive the required equations for the tip asymptotics we integrate the conservation law (Eq. (2.14)) over the tip region

$(\xi, 1)$, where $\xi \to 1$. After applying the boundary conditions (2.15), integrating by parts, and combining with Eq. (2.13), the resulting equation can be expressed in the form

$$\mathcal{G}_m^{-1}\Psi = -\mathcal{G}_m^{-1}\frac{\Omega^3}{\gamma}\frac{\partial \Pi}{\partial \xi} = \xi\dot{\gamma}\Omega + \frac{\partial}{\partial \tau}\left(\gamma\int_{\xi}^{1}\Omega\left(\xi',\tau\right)d\xi'\right). \tag{2.20}$$

2.3.1. Viscosity dominated asymptote

Assuming $\mathcal{G}_k \ll 1$ and the following power–law behavior for Ω

$$\Omega(\xi,\tau) = A(\tau)(1-\xi)^{\alpha},\ 0<\alpha<1 \tag{2.21}$$

the asymptotic analysis of the elasticity Eq. (2.12) presented in Appendix A yields the corresponding behavior for Π

$$\Pi(\xi,\tau) = \frac{1}{4\gamma}A(\tau)\alpha\ \cot\ \pi\alpha(1-\xi)^{\alpha-1}. \tag{2.22}$$

Substituting Eqs. (2.21) and (2.22) into Eq. (2.20) and applying a dominant balance argument yields

$$\alpha = 2/3,\ A(\tau) = 2^{1/3}3^{5/6}\left(\mathcal{G}_m\gamma^2\dot{\gamma}\right)^{1/3}. \tag{2.23}$$

This is the so-called SCR asymptote [12], which we have presented here in order to establish the correct expression for $A(\tau)$ to be used for the numerical scheme.

2.3.2. Toughness dominated asymptote

In this case $\alpha = 1/2$ for which the corresponding pressure vanishes according to Eq. (2.22) so that the pressure variation, which causes the fluid in the fracture to move, must come from a higher order term. Substituting Eq. (2.17) into Eq. (2.20) and solving the resulting ODE for Π yields

$$\Pi = \dot{\gamma}\mathcal{G}_m\mathcal{G}_k^{-2}\log|1-\xi|. \tag{2.24}$$

Now making use of the asymptotic analysis presented in Appendix A, it is possible to determine the next term in the expansion for Ω corresponding to the log term in the pressure

$$\Omega = \mathcal{G}_k\gamma^{1/2}(1-\xi)^{1/2} + 4\pi\gamma\dot{\gamma}\mathcal{G}_m\mathcal{G}_k^{-2}(1-\xi).$$

These are the first two terms of the asymptotic series which can be found in [17,25].

3. Hermite cubic collocation scheme

In this section we outline the novel collocation scheme to approximate the coupled system of integro-partial differential equations, boundary, and propagation conditions (2.12)–(2.17). We partition the interval $[-1, 1]$ into N sub-intervals or elements $[\xi_k, \xi_{k+1}]$, $k = 1{:}N$ with lengths $\Delta\xi_k = |\xi_{k+1} - \xi_k|$, where $-1 = \xi_1 < \xi_2 < \ldots < \xi_N < \xi_{N+1} = 1$. Consistent with the power–law tip behavior established above, we will allow for an arbitrary power–law representation for the crack opening Ω in the first and last elements $[\xi_1, \xi_2]$ and $[\xi_N, \xi_{N+1}]$, which corresponds to the leading order asymptotic behavior given in Eq. (2.21). Within the interior elements $k = 2{:}N-1$ we will assume a representation of Ω in terms of the classic Hermite cubic basis functions [11]. Rather than adopting the element-wise assembly of the basis functions commonly used in the finite element literature, we will adopt a node based approach to facilitate the implementation of the removable singularities that occur at the self and nearest neighbor nodes. In order to ensure that the representation maintains C^1 continuity throughout, we construct blended basis functions for first and last interior mesh points ξ_1 and ξ_N by taking the appropriate linear combination of the Hermite basis functions.

For the approximation of the singular integral Eq. (2.12) we substitute the representation for Ω described above into the integral equation. The resulting equation is then reduced to a system of algebraic equations for the unknown crack opening field Ω and its gradient Ω' by collocation at the interior nodal points ξ_k, $k = 2{:}N$ and the interior element midpoints $\xi_{k+\frac{1}{2}} = (\xi_{k+1} + \xi_k)/2, k = 2{:}N-1$. The coefficient matrices for this system of equations are evaluated by determining the integrals of the singular integral operator (Eq. (2.12)) applied to the basis functions. These integrals, which we will refer to as 'influence functions', are evaluated in closed form and presented below. Of particular interest is the tip element influence function for an arbitrary power–law, which can be used to track hydraulic fracture evolution for a number of different propagation regimes. Since all hydraulic fractures are not governed by integral equations with the hypersingular/Cauchy kernel considered here, the applicability of these influence functions would seem to be limited to this special case. However, since the hypersingular kernel (Eq. (2.12)) appears as the dominant part of a large number of crack propagation problems, these influence functions can be used to treat the singular part of a large number of fracture propagation situations while the contribution to influence functions of the regular, subdominant components can be treated by standard numerical quadrature. For a number of one dimensional examples in which this situation occurs see [24], while the analysis presented in [30] demonstrates that the two-dimensional elasticity operator can be shown to reduce to the form (Eq. (2.12)) close to the periphery of a planar fracture with a smooth boundary.

For the spatial discretization of the coupled PDEs (Eqs. (2.13)–(2.14)) we make use of a fourth order collocation scheme [7,21], which is based on the same Hermite cubic interpolation used to discretize the integral Eq. (2.12).

3.1. Hermite cubic basis functions and interpolation formulae

3.1.1. Basis functions

As described above we assume the following representation of Ω in terms of translates of the classic Hermite cubic basis functions H^0 (which are associated with the nodal values Ω_k) and H^1 (which are associated with the nodal derivatives Ω_k'), and the blended cubic Hermite-power–law basis functions H_-^e and H_+^e (associated with the tip power–law values Ω_2 and Ω_N, respectively). The expansion for Ω assumes the form:

$$\begin{aligned}\Omega(\xi) = &\sum_{k=3}^{N-1}\Omega_k H^0(\xi-\xi_k,\Delta_{k-1},\Delta_k) + \Omega_k' H^1(\xi-\xi_k,\Delta_{k-1},\Delta_k)\\ &+ \Omega_2 H_-^e(\xi-\xi_2,\Delta_1,\Delta_2,\alpha) + \Omega_N H_+^e(\xi-\xi_N,\Delta_{N-1},\Delta_N,\alpha)\end{aligned} \tag{3.1}$$

where the explicit expressions for these basis functions are:

$$H^0(s,\Delta_-,\Delta_+) = \begin{cases} H_-^0(s,\Delta_-) = \left(-2s^3-3s^2\Delta_- + \Delta_-^3\right)/\Delta_-^3,\ \text{for } s\in[-\Delta_-,0)\\ H_+^0(s,\Delta_+) = \left(2s^3-3s^2\Delta_+ + \Delta_+^3\right)/\Delta_+^3,\ \text{for } s\in[0,\Delta_+]\\ 0,\ \text{for } s\notin[-\Delta_-,\Delta_+]\end{cases} \tag{3.2}$$

and

$$H^1(s,\Delta_-,\Delta_+) = \begin{cases} H_-^1(s) = \left(s^3-2s^2\Delta_- + s\Delta_-^2\right)/\Delta_-^2,\ \text{for } s\in[-\Delta_-,0)\\ H_+^1(s) = \left(s^3+2s^2\Delta_+ + s\Delta_+^2\right)/\Delta_+^2,\ \text{for } s\in[0,\Delta_+]\\ 0,\ \text{for } s\notin[-\Delta_-,\Delta_+]\end{cases}. \tag{3.3}$$

We have chosen to express H^0 and H^1 in expanded polynomial form to facilitate the evaluation of the influence integrals. Moreover, $H^0_\pm$ and $H^1_\pm$ have been used to denote the left and right partial basis functions that are used to construct H^0 and H^1, respectively. The blended cubic Hermite-power–law basis functions $H^e_\pm$ will be defined in subsection 3.2. As an illustration, the Hermite cubic basis functions $H^0(s, 2, 1)$ and $H^1(s, 2, 1)$ defined on the interval $[-\Delta_-, \Delta_+]=[-2, 1]$ are plotted in Fig. 1(a).

3.1.2. Interpolation formulae

For the implementation of the coupled approximation scheme it is necessary to determine expressions for Ω and Ω' at the interior element halfpoints $\xi_{k+\frac{1}{2}} = (\xi_{k+1} + \xi_k)/2, k = 2 : N-1$. Assuming that the nodal function values $\{\Omega_k, \Omega_{k+1}\}$ and derivatives $\{\Omega'_k, \Omega'_{k+1}\}$ are known, the Hermite cubic representation yields the following fourth order approximation to $\Omega_{k+\frac{1}{2}}$

$$\Omega_{k+\frac{1}{2}} = \frac{1}{2}(\Omega_{k+1} + \Omega_k) - \frac{\Delta s_k}{8}\left(\Omega'_{k+1} - \Omega'_k\right) + O\left(\Delta s_k^4\right) \tag{3.4}$$

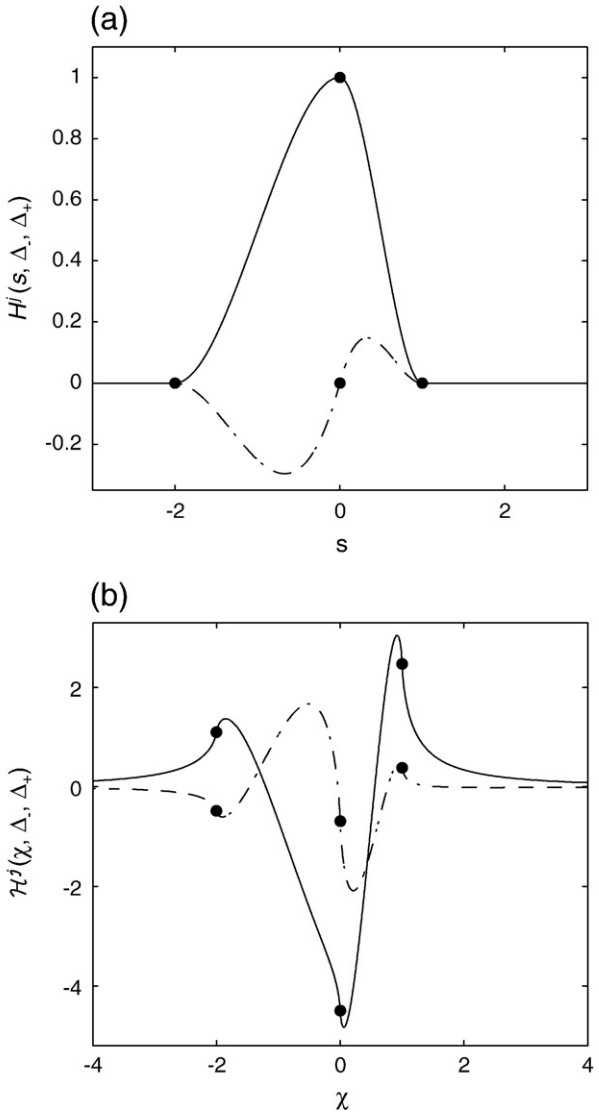

Fig. 1. (a) Top figure: plot of $H^0(s, \Delta_-, \Delta_+)$ (solid curve) and $H^1(s, \Delta_-, \Delta_+)$ (-. curve) versus s for $[-\Delta_-, \Delta_+]=[-2, 1]$. (b) Bottom figure plot of the corresponding influence functions $H^0(\chi, \Delta_-, \Delta_+)$ (solid curve) and $\mathcal{H}^1(\chi, \Delta_-, \Delta_+)$ (-. curve) versus χ (defined in Section 3.3). The nodal points corresponding to the self effect point $\chi=0$ and the nearest neighbor points $\chi=\Delta_\pm$ are denoted by the solid circles.

and the corresponding approximation to $\Omega'_{k+\frac{1}{2}}$

$$\Omega'_{k+\frac{1}{2}} = \frac{3}{2}\left(\frac{\Omega_{k+1}-\Omega_k}{\Delta s_k}\right) - \frac{1}{4}\left(\Omega'_{k+1} + \Omega'_k\right) + O\left(\Delta s_k^4\right). \tag{3.5}$$

3.2. Blended cubic Hermite-power–law basis functions for tip elements

In order to construct a basis function appropriate for an arbitrary power–law

$$\Omega(\xi) = A(1-\xi)^\alpha$$

we consider a shifted coordinate $s=\xi-\xi_N$ so that $1-\xi=\Delta\xi_N-s$, from which it follows that

$$\Omega(\xi) = A\Delta\xi_N^\alpha(1-s/\Delta\xi_N)^\alpha.$$

Observing that $\Omega(\xi_N)=A\Delta\xi_N^\alpha$ and that the power–law function $(1-s/\Delta\xi_N)^\alpha$ is unity at $s=0$, we define the blended cubic Hermite-power–law basis function appropriate for the rightmost interior node ξ_N as

$$H^e_+(s, \Delta_-, \Delta_+, \alpha) = \begin{cases} H^0_-(s, \Delta_-) - \dfrac{\alpha}{\Delta_+} H^1_-(s, \Delta_-), & \text{for } s\in[-\Delta_-, 0) \\ (1-s/\Delta_+)^\alpha, & \text{for } s\in[0, \Delta_+] \\ 0, & \text{for } s\notin[-\Delta_-, \Delta_+] \end{cases}. \tag{3.6}$$

Similarly, the appropriate blended basis function for the leftmost interior node ξ_2 is given by

$$H^e_-(s, \Delta_-, \Delta_+, \alpha) = \begin{cases} (1+s/\Delta_-)^\alpha, & \text{for } s\in[-\Delta_-, 0) \\ H^0_+(s, \Delta_+) + \dfrac{\alpha}{\Delta_-} H^1_+(s, \Delta_+), & \text{for } s\in[0, \Delta_+] \\ 0, & \text{for } s\notin[-\Delta_-, \Delta_+] \end{cases}. \tag{3.7}$$

As an illustration, the blended cubic Hermite-power–law basis function $H^e_+(s, 2, 1, \alpha)$ defined on the interval $[-\Delta_-, \Delta_+]=[-2, 1]$ is plotted in Fig. 2(a) for the case $\alpha=1/2$.

3.3. Influence functions

The influence function $\mathcal{H}^j$, corresponding to one of the basis functions $H^j(s)$ described in the previous subsection, is defined to be

$$\mathcal{H}^j(\chi) = \oint_{-\Delta_-}^{\Delta_+} \frac{H^j(s)}{(s-\chi)^2} ds = \oint_{-\Delta_-}^{\Delta_+} \frac{\partial H^j(s)}{\partial s} \frac{1}{s-\chi} ds. \tag{3.8}$$

We note that the equivalence of the two integral operators in Eq. (3.8) holds because the basis functions $H^j(s)$ all vanish at the endpoints of the integration interval. Here $s\in[-\Delta_-, \Delta_+]$ represents a local coordinate system centered on the node of interest and χ represents the receiving point relative to this local coordinate system. The influence function $\mathcal{H}^j$ represents the scaled stress field generated at point χ due to a crack whose width profile is given by the basis function defined by $H^j(s)$. We have chosen to exclude factor $-\frac{1}{4\pi\gamma}$ from the definition of these influence functions so as

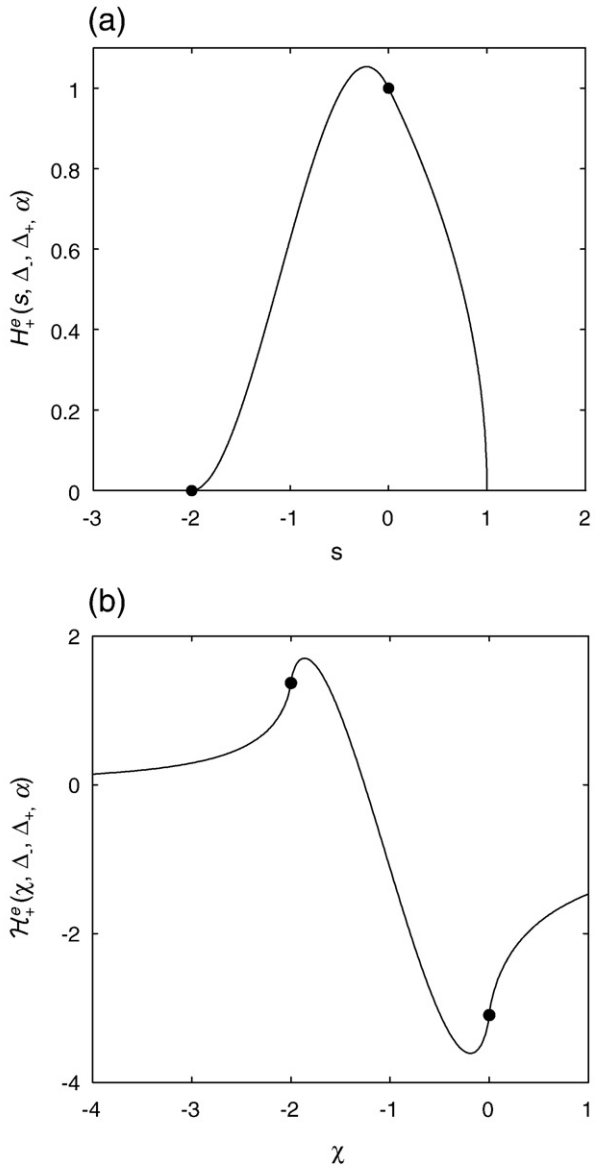

Fig. 2. (a) Top figure: plot of the right tip blended basis function $H^e_+(s, \Delta_-, \Delta_+, \alpha)$ versus s for $[-\Delta_-, \Delta_+]=[-2, 1]$ and $\alpha=1/2$. (b) Bottom figure plot of the corresponding influence function $\mathcal{H}^e_+(\chi, \Delta_-, \Delta_+, \alpha)$ versus χ (defined in Section 3.3). The nodal points corresponding to the self effect point $\chi=0$ and the nearest neighbor point $\chi=\Delta_-$ are denoted by the solid circles.

not to clutter the formulae unnecessarily and which can be added *a posteriori*.

3.3.1. Interior elements

The expression for the influence function $\mathcal{H}^0$ is given by

$$\mathcal{H}^0(\chi,\Delta_-,\Delta_+) = -3\left(\frac{1}{\Delta_+}+\frac{1}{\Delta_-}\right)+6\chi\left(\frac{1}{\Delta_+^2}-\frac{1}{\Delta_-^2}\right) + \frac{6\chi(\chi-\Delta_+)}{\Delta_+^3}\log\left|\frac{\chi-\Delta_+}{\chi}\right| + \frac{6\chi(\chi+\Delta_-)}{\Delta_-^3}\log\left|\frac{\chi+\Delta_-}{\chi}\right| \tag{3.9}$$

while the expression for $\mathcal{H}^1$ is given by

$$\mathcal{H}^1(\chi,\Delta_-,\Delta_+) = \left(\frac{1}{\Delta_+}+\frac{1}{\Delta_-}\right)\left[3\chi+4\chi\log|\chi|\right] -3\left(\frac{1}{\Delta_+^2}-\frac{1}{\Delta_-^2}\right)\chi^2\log|\chi| + \frac{(3\chi-\Delta_+)(\chi-\Delta_+)}{\Delta_+^2}\log|\chi-\Delta_+ - \frac{(3\chi+\Delta_-)(\chi+\Delta_-)}{\Delta_-^2}\log|\chi+\Delta_-. \tag{3.10}$$

The influence functions $\mathcal{H}^0(\chi, 2,1)$ and $\mathcal{H}^1(\chi, 2,1)$ corresponding to the interval $[-\Delta_-, \Delta_+]=[-2, 1]$ are plotted in Fig. 1(b). The nodal points corresponding to the self effect point $\chi=0$ and the nearest neighbor points $\chi=\Delta_\pm$ are denoted by the solid circles.

3.3.1.1. Self and nearest neighbor influences. The self effect $\chi=0$ and nearest neighbor influences $\chi=\Delta_\pm$ are all finite and can be determined directly from Eqs. (3.9) and (3.10) by taking the appropriate limits. It is also interesting to note that by taking the far-field limit $\chi\to\infty$ it can be shown that the influence functions decay as $O(\frac{1}{\chi^2})$ as is to be expected from the asymptotic behavior of the hypersingular integral operator (Eq. (2.12)) as $\xi\to\infty$.

3.3.2. Tip elements

The influence function associated with the blended cubic Hermite-power–law basis function H^e_+ for values of α in the range $0<\alpha<1$, can be expressed in the following form

$$\mathcal{H}^e_+(\chi,\Delta_-,\Delta_+,\alpha) = -\frac{3}{\Delta_-}-\frac{6\chi}{\Delta_-^2}+\frac{6\chi(\chi+\Delta_-)}{\Delta_-^3}\log\left|\frac{\chi+\Delta_-}{\chi}\right| -\frac{\alpha}{\Delta_+}\left(\frac{3\chi}{\Delta_-}+\frac{5}{2}-\frac{(3\chi+\Delta_-)(\chi+\Delta_-)}{\Delta_-^2}\log\left|\frac{\chi+\Delta_-}{\chi}\right|\right) -\frac{\alpha}{\Delta_+}(1-\chi/\Delta_+)^{\alpha-1}\left[\pi\cot\pi\alpha+ReB_{(1-\chi/\Delta_+)}(1-\alpha,0)\right] \tag{3.11}$$

where $B_z(a, b)$ is the incomplete Beta function [1] defined by

$$B_z(a,b) = \int_0^z t^{a-1}(1-t)^{b-1}dt. \tag{3.12}$$

We observe that as $z\to 1$, $B_z(1-\alpha, 0)$ has a logarithmic singularity, which cancels with the other logarithmic terms in Eq. (3.11) to yield a stress field that is finite at the points $\chi=0, -\Delta_-$. In order to evaluate $\mathcal{H}^e_+(\chi, \Delta_-, \Delta_+, \alpha)$ over the full range of values of χ, we need to evaluate $B_z(a, b)$ for values of $z>1$ — for which the definition (3.12) is inappropriate. In this case we obtain the analytic continuation of the incomplete Beta function provided by its expression in terms of Gauss' Hypergeometric Function ${}_2F_1$ see [1]. The required identity is given by

$$B_z(1-\alpha,0) = \frac{1}{1-\alpha}z^{1-\alpha}{}_2F_1{}^2(1-\alpha,1,2-\alpha;z).$$

Finally, we observe that the singular term $-\frac{\alpha}{\Delta_+}(1-\chi/\Delta_+)^{\alpha-1}\pi\cot\pi\alpha$ agrees exactly with the leading behavior of the integral equation obtained by the local analysis provided in Appendix A. The influence function $\mathcal{H}^e_+(\chi, 2, 1, \alpha)$ corresponding to the interval $[-\Delta_-, \Delta_+]=[-2, 1]$ and $\alpha=1/2$ is plotted in Fig. 2(b). The nodal

points corresponding to the self effect point $\chi=0$ and the nearest neighbor point $\chi=\Delta_-$ are denoted by the solid circles. We observe that the stress field at the tip of this element $\chi=1$, which would correspond to the tip of the fracture, is finite because of the choice $\alpha=1/2$. It is clear from Eq. (3.11) that any other choice of $\alpha<1$ will result in an infinite stress field at this point. A similar expression can be obtained for the influence function $\mathcal{H}^e_-(\chi,\ \Delta_-,\ \Delta_+,\ \alpha)$ corresponding to $H^e_-(s,\ \Delta_-,\ \Delta_+\ \alpha)$ — the blended basis function associated with the leftmost interior node.

3.3.2.1. Self influence. Because the expression for $\mathcal{H}^e_+(\chi,\ \Delta_-,\ \Delta_+,\ \alpha)$ involves special functions, the self effect cannot be obtained by inspection. To obtain an expression for the self influence we make use of the following asymptotic expansion for the incomplete Beta function

$$B_z(1-\alpha,0) \overset{z\to 1_-}{=} [-\gamma_E-\psi(1-\alpha)-\log|1-z|] + O(1-z) \tag{3.13}$$

where $\gamma_E\approx 0.57722$ is Euler's constant and ψ is the polygamma function (see [1]). Making use of the expansion (3.13) and simplifying terms we obtain the following expression for the self influence

$$\mathcal{H}^e_+(0,\Delta_-,\Delta_+,\alpha) = -\frac{3}{\Delta_-}-\frac{5\alpha}{2\Delta_+}-\frac{\alpha}{\Delta_+}\left(\pi\cot\pi\alpha+\log\left|\frac{\Delta_+}{\Delta_-}\right|-\gamma_E-\psi(1-\alpha)\right).$$

3.3.2.2. Nearest neighbor influence. The nearest neighbor influence can be obtained directly from Eq. (3.11) by taking the appropriate limit, which yields

$$\mathcal{H}^e_+(-\Delta_-,\Delta_-,\Delta_+,\alpha) = \frac{3}{\Delta_-}+\frac{\alpha}{2\Delta_+}-\frac{\alpha}{\Delta_+}(1+\Delta_-/\Delta_+)^{\alpha-1} \times\left(\pi\cot\pi\alpha+ReB_{(1+\Delta_-/\Delta_+)}(1-\alpha,0)\right).$$

3.4. Collocation approximation scheme

Having developed the necessary approximations for the integral equation, we are now in a position to describe the proposed collocation scheme to determine the unknown functions Ω, Ω', Π, Ψ, and γ. We choose to describe the algorithm for the evolution of a *symmetric crack* and restrict our discretization to the right sub-interval [0, 1]. We partition the interval [0, 1] into M sub-intervals or elements $[\xi_k,\xi_{k+1}]$, $k=1{:}M$ where $0=\xi_1<\xi_2<\ldots<\xi_M<\xi_{M+1}=1$. This mesh corresponds to that described above in the case $N=2M$. For this mesh the following $4M+1$ unknowns need to be determined

$$\left\{\Omega=\Omega_1,\ldots,\Omega_M;\Omega'=\Omega'_1,\ldots,\Omega'_M;\Pi=\Pi_1,\ldots,\Pi_M;\Psi=\Psi_1,\ldots,\Psi_M;\gamma\right\}.$$

Conceptually the interval $[0,\ 1]=[0,\ \xi_M)\cup[\xi_M,\ 1]$ is split at the point ξ_M into an interior region and a tip region. This decomposition is necessary because of the anticipated singular behavior of the unknown fields as we approach the tip $\xi\to 1$, which we established via the asymptotic analysis presented in subsection 2.3. Approximations based on piecewise polynomials that did not include the singular tip would be inaccurate. Therefore in the tip region we have chosen to use the leading term in the asymptotic expansion of the solution, while in the interior region, where the solution is expected to be regular, we will deploy the standard piecewise cubic approximation. The interface point ξ_M between these two regions becomes the point at which the 'boundary conditions' for the interior problem are prescribed. We now present the $4M+1$ equations and boundary conditions that are required to determine the solution.

3.4.1. Differential equation approximation

In order to express the differential equations in the problem as a system in a more standard form, we rewrite Poiseuille's Law (Eq. (2.13)) and the mass conservation law (Eq. (2.14)) as follows

$$\frac{\partial\Pi}{\partial\xi} = -\frac{\gamma\Psi}{\Omega^3} = F_\Pi\left(\Omega,\Omega',\Pi,\Psi,\gamma\right) \tag{3.14}$$

$$\frac{\partial\Psi}{\partial\xi} = \mathcal{G}_m\left(\dot\gamma\xi\Omega'-\gamma\dot\Omega\right) = F_\Psi\left(\Omega,\Omega',\Pi,\Psi,\gamma\right). \tag{3.15}$$

We observe that Ω and Ω' are primary variables that are determined by the integral equation — provided the appropriate pressure field Π is known. In the definition of the gradient functions F_Π and F_Ψ and their stated dependence on Ω, Ω', Π, Ψ, and γ, we have assumed that the time derivatives have been replaced by first order backward difference quotients

$$\dot\Omega = \frac{\Omega-\Omega_{\tau-\Delta\tau}}{\Delta\tau},\dot\gamma = \frac{\gamma-\gamma_{\tau-\Delta\tau}}{\Delta\tau}$$

This time discretization amounts to a Backward Euler time-stepping scheme, whose L-stability is desirable due to the stiffness of the equations. Higher order accuracy for the time discretization can be achieved by using an appropriate higher order backward difference scheme. For the sake of brevity we will restrict our description to the spatial discretization, which is the novel part of the algorithm. Previous approaches to this class of coupled problems [14] have involved finite difference or finite volume discretizations of the lubrication Eq. (2.5). The integral Eq. (2.2) is typically discretized using collocation and assuming a piecewise constant or a non-conforming piecewise-linear representation of Ω in which the collocation points correspond to the mesh points of the finite difference scheme. Alternative discretizations of the integral equation have involved Gauss–Chebyshev quadrature in which the integration points correspond to those of the finite difference mesh [10]. None of these methods allow for explicit incorporation of the type of power–law behavior typically encountered in hydraulic fracture problems and rely upon specialized upwind differencing to treat the convective terms in the scaled lubrication equation. The spatial discretization scheme proposed in this paper allows for the treatment of arbitrary power–law tip behavior as well as a unified treatment of the discretization of the lubrication equation and the elastic integral equation in terms of Hermite cubic basis functions. Since the convective term becomes a primary variable in this scheme no specialized treatment is required.

Following [7,21] we integrate Eqs. (3.14)–(3.15) over a typical element and use Simpson's Rule to approximate the resulting integrals in order to obtain the following collocation equations

$$\Pi_{k+1} = \Pi_k + \frac{\Delta\xi_k}{6}\left(F_{\Pi,k}+4F_{\Pi,k+\frac12}+F_{\Pi,k+1}\right),\ k=1:M-1 \tag{3.16}$$

$$\Psi_{k+1} = \Psi_k + \frac{\Delta\xi_k}{6}\left(F_{\Psi,k}+4F_{\Psi,k+\frac12}+F_{\Psi,k+1}\right),\ k=1:M-1. \tag{3.17}$$

In order to evaluate $F_{\Pi,k+\frac12}$ and $F_{\Psi,k+\frac12}$, the interpolation formulae (3.4)–(3.5) are used to determine $\Omega_{k+\frac12}$ and $\Omega'_{k+\frac12}$ respectively, while $\Pi_{k+\frac12}$ is determined using the same interpolation formula as Eq. (3.4), but using the ODE for Π to provide the gradients, i.e.,

$$\Pi_{k+\frac12} = \frac12(\Pi_{k+1}+\Pi_k)-\frac{\Delta\xi_k}{8}\left(F_{\Pi,k+1}-F_{\Pi,k}\right). \tag{3.18}$$

An analogous equation is used to determine $\Psi_{k+\frac12}$.

3.4.2. Integral equation approximation

Having introduced the cubic Hermite basis function representation (3.1) of Ω and the corresponding influence functions, the discretized integral equation can be expressed in the form

$$\gamma\Pi_k = \sum_{l=1}^{M} C^0_{kl}\Omega_l + \sum_{l=1}^{M-1} C^1_{kl}\Omega'_l,\ k = 1:M \tag{3.19}$$

where

$$\begin{aligned} C^0_{k1} &= \lambda\mathcal{H}^0(\xi_k - \xi_1, \Delta_1, \Delta_1) \\ C^0_{kl} &= \lambda\mathcal{H}^0(\xi_k - \xi_l, \Delta_{l-1}, \Delta_l) + \lambda\mathcal{H}^0(\xi_k + \xi_l, \Delta_l, \Delta_{l-1}),\ l = 2:M-1 \\ C^0_{kM} &= \lambda\mathcal{H}^e_+(\xi_k - \xi_M, \Delta_{M-1}, \Delta_M, \alpha) + \lambda\mathcal{H}^e_-(\xi_k + \xi_M, \Delta_M, \Delta_{M-1}, \alpha) \end{aligned} \tag{3.20}$$

and

$$\begin{aligned} C^1_{k1} &= \lambda\mathcal{H}^1(\xi_k - \xi_1, \Delta_1, \Delta_1) \\ C^1_{kl} &= \lambda\mathcal{H}^1(\xi_k - \xi_l, \Delta_{l-1}, \Delta_l) - \lambda\mathcal{H}^1(\xi_k + \xi_l, \Delta_l, \Delta_{l-1}),\ l = 2:M-1 \end{aligned} \tag{3.21}$$

and $\lambda = -\frac{1}{4\pi}$. We note that, other than the two coefficient functions associated with the node at the origin $x_1 = 0$, all the coefficient functions C^j_{kl} defined in Eqs. (3.20)–(3.21) involve two influence functions, one due to the basis function to the right of the origin and the other from the image basis function to the left of the origin. In this way symmetry is embedded in the discrete elasticity Eq. (3.19) and the left wing of the crack does not require any computational resources. An equivalent formulation would be to build the image effects into the kernels of the integral equation itself. In order to maintain flexibility, we have chosen not to use this approach, as the expressions for the kernel functions given in this paper can be used for problems without symmetry as well as for symmetric problems by simply including the image elements. To complete the system of equations we also choose to collocate the integral equation at the midpoints of the elements, resulting in the following system of equations

$$\gamma\Pi_{k+\frac{1}{2}} = \sum_{l=1}^{M} C^0_{k+\frac{1}{2}l}\Omega_l + \sum_{l=1}^{M-1} C^1_{k+\frac{1}{2}l}\Omega'_l,\ k = 1:M-1. \tag{3.22}$$

Here $C^0_{k+\frac{1}{2}l}$ and $C^1_{k+\frac{1}{2}l}$ are precisely the same functions as those given in Eqs. (3.20) and (3.21) but with ξ_k replaced by $\xi_{k+\frac{1}{2}}$. The values of $\Pi_{k+\frac{1}{2}}$ at the element midpoints are determined by the interpolation formula (3.18).

3.4.3. Approximate global volume balance

The global volume balance condition (2.16) is approximated in two parts. On the interior sub-interval $[0, \xi_M)$ we use a Simpson's Rule approximation that is consistent with that used to discretize the differential equations. The volume of fluid in the tip region $[\xi_M, 1]$ is evaluated analytically by integrating the asymptotic relation (2.21). The resulting discrete form of the volume balance condition (2.16), is as follows

$$\mathcal{G}_v\tau = 2\gamma\left[\sum_{k=1}^{M-1}\frac{\Delta\xi_k}{6}\left(\Omega_k + 4\Omega_{k+\frac{1}{2}} + \Omega_{k+1}\right) + A(\tau)\frac{\Delta\xi_M^{\alpha+1}}{\alpha+1}\right]. \tag{3.23}$$

3.4.4. Boundary conditions

The boundary conditions for the interior problem involve the prescribed flux at the source point ξ_1 and the values of Ω and Ω' at the interface point ξ_M, namely

$$\Psi_1 = \frac{\mathcal{G}_m\mathcal{G}_v}{2},\ \Omega_M = A(\tau)\Delta\xi_M^{\alpha},\ \Omega'_M = A(\tau)\alpha\Delta\xi_M^{\alpha-1}. \tag{3.24}$$

3.4.5. Solution of the nonlinear equations

The $4M+1$ nonlinear Eqs. (3.16), (3.17), (3.19), (3.22), (3.23), and (3.24) that determine the $4M+1$ unknowns $\{\mathbf{\Omega}; \mathbf{\Omega'}; \mathbf{\Pi}; \mathbf{\Psi}; \gamma\}$ are solved iteratively using a Newton scheme in which the Jacobian is evaluated numerically by divided differences (see for example [7]). The incorporation of the correct tip asymptotic behavior assists with the selection of the appropriate solution so that the Newton scheme typically converges in no more than three iterations.

4. Numerical results

In this section we present results demonstrating the performance of the proposed algorithm for a number of test problems. The first test problem considers the propagation of a plane strain crack in an elastic medium with zero toughness. This problem has been chosen because there is a similarity solution with which it is possible to compare the cubic Hermite algorithm and to explore its convergence properties. The second test problem involves propagation in a large toughness regime in which the dimensionless viscosity is very small. This problem has an asymptotic expansion in powers of the small dimensionless viscosity with which the cubic Hermite solution can be compared. The third test problem involves the buoyancy driven propagation of a hydraulic fracture for large dimensionless toughness. This problem is chosen to demonstrate the application of the method to a semi-infinite crack problem — a class of reduced problem frequently considered in the asymptotic analysis of hydraulic fractures. We compare the cubic Hermite solution to results published in [32].

4.1. Propagation of crack in a medium with zero toughness

In the first test problem we consider the propagation of a KGD fracture in a medium with zero toughness and compare the solutions produced by the Hermite collocation scheme with the analytic solution due to Carbonell [9] (also see [5] for a more efficient implementation generalized to power–law fluids). For this problem $\mathcal{G}_k = 0$, and we assume the viscosity scaling and use the viscosity dominated tip asymptote given by Eq. (2.23).

In this experiment we initialize the numerical solution to the Carbonell solution at the dimensionless time horizon $\tau = \tau_0 = 1$. In order to enable us to explore the accuracy of the spatial discretization, which is the focus of this paper, we assume a very small time-step $\Delta\tau = 0.01$. This choice is made in order to ensure that the errors due to the first order Backward Euler time-stepping scheme remain subdominant to those of the spatial discretization scheme. In Fig. 3 we compare the fracture apertures Ω and fluid pressures Π obtained by using the Hermite collocation algorithm using $M = 20$ nodes with those of the analytic solution at four distinct points in time $\tau = 10$, 50, 200, and 600. There is close agreement between the two solutions. In Fig. 4(a) we plot the fracture aperture at time $\tau = 10$ when $M = 5$, 10, and 20 nodes were used. In Fig. 4(b) we plot the corresponding relative errors in the fracture aperture expressed as a percentage. The Hermite cubic solutions clearly converge to the exact solution. Similar orders of error were obtained at later times. In Fig. 5(a) we demonstrate the asymptotic behavior of the error at $\Omega(0, 10)$ (which is the point at which the relative error is a maximum over the interval [0, 1] as can be seen from Fig. 3). A linear regression on the

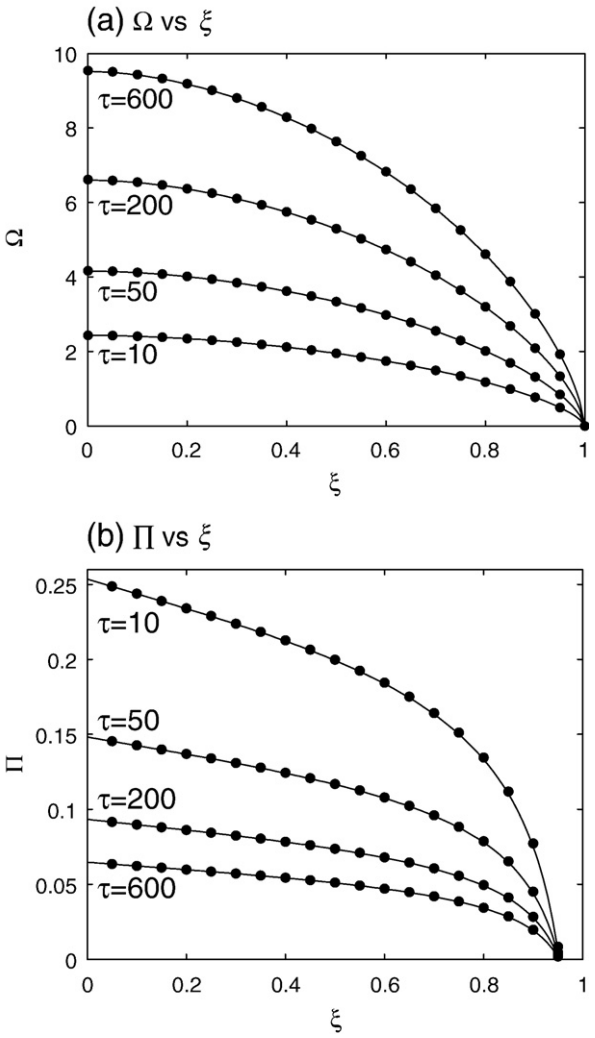

Fig. 3. Top figure: comparison of Hermite cubic fracture widths at the $M=20$ collocation points denoted by solid circles with the corresponding exact fracture widths denoted by the solid lines at dimensionless times $\tau=10$, 50, 200, and 600. The fracture widths Ω increase monotonically with time. Bottom figure: comparison of Hermite cubic fluid pressures at the $M=20$ collocation points denoted by solid circles with the corresponding exact fluid pressures denoted by the solid lines at dimensionless times $\tau=10$, 50, 200, and 600. The fluid pressures Π decrease monotonically with time.

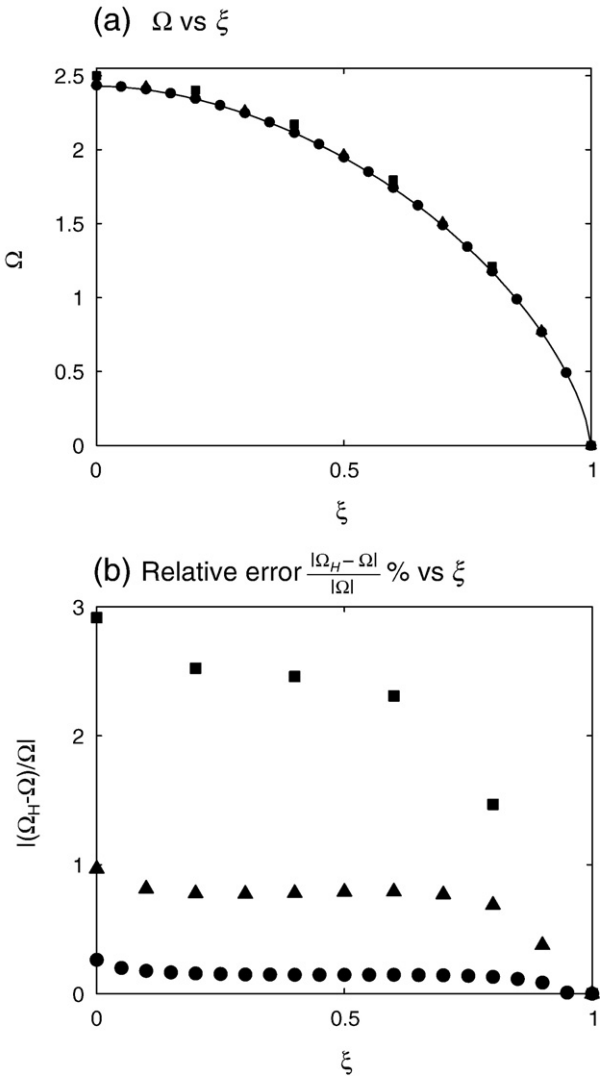

Fig. 4. Top figure: comparison of Hermite cubic fracture widths sampled at the dimensionless time $\tau=10$ using discretizations with $M=5$ (squares), $M=10$ (triangles), and $M=20$ (circles) and the corresponding exact fracture widths denoted by the solid line. Bottom figure: the relative errors in the Hermite cubic fracture widths Ω at the dimensionless time $\tau=10$ for $M=5$, 10, and 20.

largest four mesh points yields an estimate of the initial convergence rate to be $O(\Delta\xi^{2.43})$. That this solution has not achieved the $O(\Delta\xi^4)$ accuracy expected from cubic Hermite interpolation, is due to the fact that the tip element only makes use of the leading order term in the asymptotic expansion for Ω. This error, which is made at the interface point ξ_M and propagates throughout the domain, should be of the order as the first neglected term in the asymptotic series. For $N\geq 80$ the error starts to decrease rapidly because the effect of the error in the tip asymptote becomes subdominant.

In Fig. 5(b) various Hermite cubic estimates of the fracture length corresponding to $M=5$, 10, and 20 nodes and $\Delta\tau=0.01$ are compared to the exact solution $\gamma(\tau)$ over the time interval $\tau\in[1, 600]$. The cases $M=10$ and 20 are indistinguishable at this scale from the exact solution. The cubic Hermite solution clearly converges to the exact solution. Also plotted on the same figure using solid circles are the estimates of the fracture length using the following geometric growth rule to increment the time-step $\Delta\tau_{k+1}=r\Delta\tau_k$, where $r=1.2$. The results are indistinguishable from those of the very fine uniform time-step and the same spatial resolution $M=20$. This scheme will thus be very useful for exploring the transition from one mode of fracture propagation to another, which might involve simulation over many orders of magnitude in time. Even with this dramatic increase in the time-step there is little deterioration in the quality of the solution.

4.2. Propagation of a crack in a large toughness regime

In the second test problem we consider the propagation of a KGD fracture in a medium with large toughness. In this case we assume the toughness scaling and choose the value of the dimensionless viscosity $\mathcal{G}_m=0.01$. We compare the solutions produced by the Hermite collocation scheme with the asymptotic expansion in powers of the dimensionless viscosity $\mathcal{G}_m$ due to Garagash [18]. This value of $\mathcal{G}_m$ was chosen for this experiment as it was identified by Garagash as being sufficiently small to yield accurate values for the width and pressure fields. In order to improve on the accuracy of the asymptotic solution, we used the Euler transformation derived in that paper to accelerate the convergence of the asymptotic series. This transformation amounts to replacing the small parameter $\mathcal{G}_m$ by the alternative expansion parameter $\delta=\frac{\mathcal{G}_m}{\sqrt{1+\mathcal{G}_m/\mathcal{G}_{msi}}}$ where $\mathcal{G}_{msi}\approx 0.0333$. Because the fracture is propagating in the toughness dominated regime the appropriate tip asymptote is given by Eq. (2.17).

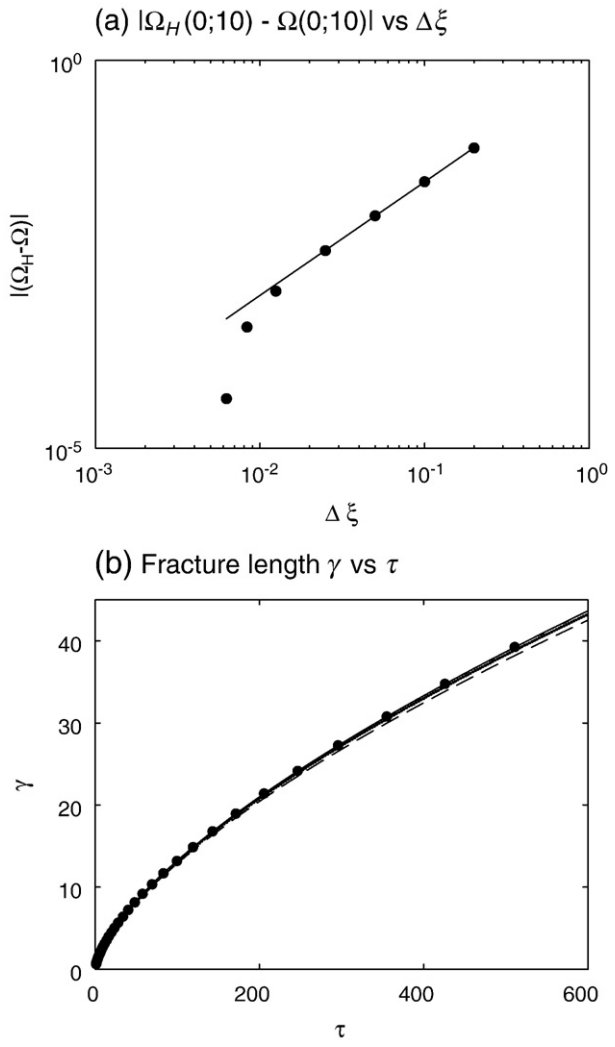

Fig. 5. Top figure: asymptotic convergence of the cubic Hermite fracture width $\Omega(0, 10)$ estimated using mesh sizes $\Delta\xi = 1/5$, 1/10, 1/20, 1/40, 1/80, 1/120, and 1/160. A linear regression on the errors for the larger four mesh sizes indicates that the asymptotic convergence rate is $O(\Delta\xi^{2.43})$. Bottom figure: comparison of the cubic Hermite fracture lengths for various spatial discretizations ($M = 5$ dashed, $M = 10$ dotted, $M = 20$ dash-dot), and the exact fracture length γ solid. Also denoted on this plot by solid circles are the fracture length estimates obtained using $M = 20$ elements and a scheme to increase the time-step size geometrically according to the rule $\Delta\tau_{k+1} = r\Delta\tau_k$, $r = 1.2$.

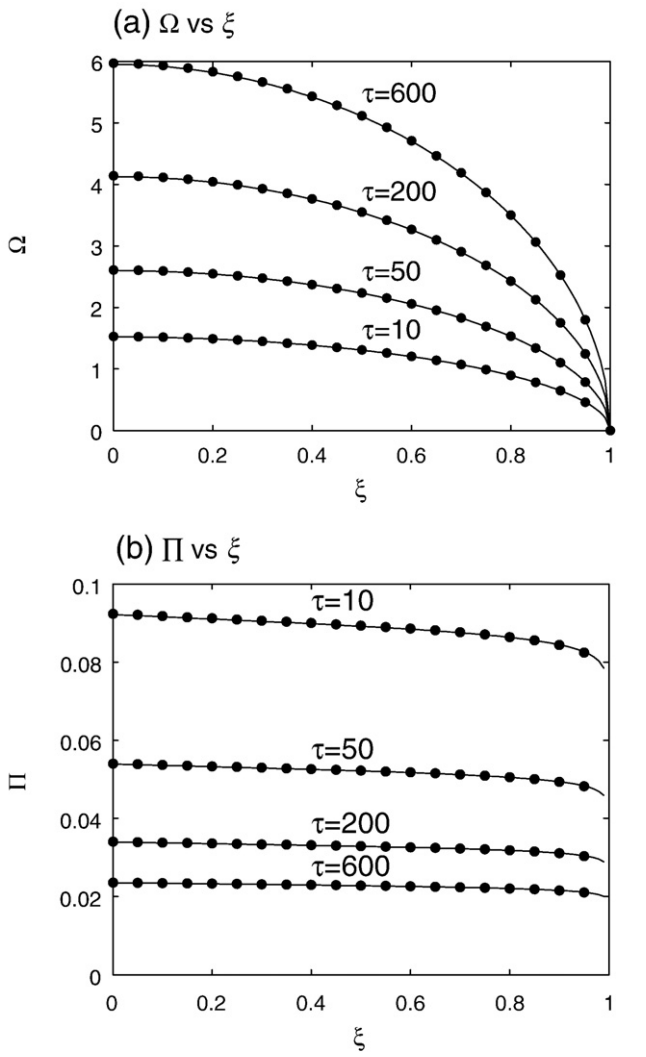

Fig. 6. Top figure: comparison of Hermite cubic fracture widths at the $M = 20$ collocation points denoted by solid circles with the corresponding two-term large toughness asymptotic solution denoted by the solid lines at dimensionless times $\tau = 10$, 50, 200, and 600. The fracture widths Ω increase monotonically with time. Bottom figure: comparison of Hermite cubic fluid pressures at the $M = 20$ collocation points denoted by solid circles with the corresponding two-term large toughness asymptotic solution denoted by the solid lines at dimensionless times $\tau = 10$, 50, 200, and 600. The fluid pressures Π decrease monotonically with time.

As in the previous experiment we initialize the numerical solution to the asymptotic solution at the dimensionless time horizon $\tau = \tau_0 = 1$ and assume a very small time-step $\Delta\tau = 0.01$ to focus on the spatial discretization errors. In Fig. 6 we compare the fracture apertures Ω and fluid pressures Π obtained by using the Hermite collocation algorithm using $M = 20$ nodes with those of the asymptotic solution at four distinct points in time $\tau = 10$, 50, 200, and 600. There is close agreement between the two solutions. This demonstrates that the performance of the Hermite scheme is not affected by the mode of propagation. We are not able to pursue a convergence study in this case since it will not be possible to distinguish between errors in the asymptotic solution and those due the numerical solution.

4.3. Propagation of buoyancy driven crack in a large toughness regime

As a third test problem we consider the model investigated by Roper and Lister [32] to explore the buoyancy driven crack propagation in the limit of large toughness. Our starting point will be first set of scaled equations that are numbered (2.7)–(2.9) in [32]:

$$p' = \frac{1}{h^2} - 1 = F_p(h, p) \tag{4.1}$$

$$p(x) = -\frac{1}{\pi}\int_0^\infty \frac{h'(s)}{s-x}\,ds \tag{4.2}$$

$$h(x) \overset{x\to 0^+}{\sim} K(2x)^{1/2}. \tag{4.3}$$

Here p represents the pressure and h the fracture half-width, i.e., $h = \Omega/2$, in the scaling presented in that paper. For the purposes of this example, we proceed to use the same symbols as those used by Roper and Lister. The methodology introduced in Section 3 can be applied directly to the approximation of Eqs. (4.1)–(4.3) with only one slight modification. In order to implement the problem on a finite truncation $[0, L]$ of the semi-infinite domain with the boundary condition,

$$h(L) = 1$$

we introduce the following blended infinite element

$$H^{\infty}(s,\Delta_{-}) = \begin{cases} H^{0}_{-}(s,\Delta_{-}), \text{ for } s\in[-\Delta_{-},0) \\ 1, \text{ for } s\in[0,\infty) \\ 0, \text{ for } s\notin[-\Delta_{-},\infty) \end{cases}$$

whose associated influence function is given by

$$\mathcal{H}^{\infty}(x,\Delta_{-}) = -\frac{3}{\Delta_{-}} - \frac{6x}{\Delta_{-}^{2}} + \frac{6x(x+\Delta_{-})}{\Delta_{-}^{3}} log\left|\frac{x+\Delta_{-}}{x}\right|. \tag{4.4}$$

We partition the interval $[0, L]$ into M sub-intervals or elements $[x_k, x_{k+1}], k=1{:}M$ where $0=x_1<x_2<\ldots<x_M<x_{M+1}=L$. For this mesh the following $3M-2$ unknowns need to be determined

$$\left\{\mathbf{h} = h_2,\ldots,h_{M+1}; h' = h'_3,\ldots,h'_M; \mathbf{p} = p_2,\ldots,p_{M+1}\right\}.$$

The discrete cubic Hermite collocation equations now assume the form

$$p_{k+1} = p_k + \frac{\Delta x_k}{6}\left(F_{p,k} + 4F_{p,k+\frac{1}{2}} + F_{p,k+1}\right),\ k=2:M$$

$$p_k = \sum_{l=2}^{M+1} C^{0}_{kl} h_l + \sum_{l=3}^{M} C^{1}_{kl} h'_l,\ k=3:M$$

$$p_{k+\frac{1}{2}} = \sum_{l=2}^{M+1} C^{0}_{k+\frac{1}{2}} l^{h}_{l} + \sum_{l=2}^{M} C^{1}_{k+\frac{1}{2}} l^{h'}_{l},\ k=2:M$$

which, along with the following two boundary conditions,

$$h_2 = K(2\Delta x_1)^{1/2} \text{ and } h_{M+1} = 1$$

provide the required $3M-2$ equations. The elasticity coefficient matrix components C^{j}_{kl} are defined in terms of the influence functions

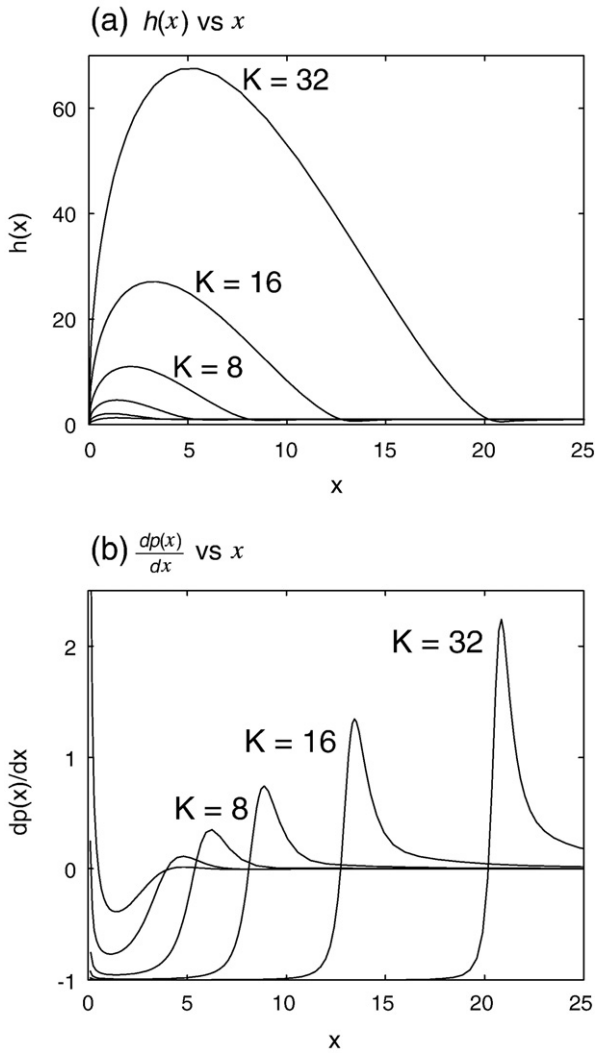

Fig. 7. Top figure: the Hermite cubic collocation fracture half-widths $h(x)$ for $K=1, 2, 4, 8, 16$, and 32 are plotted. In all these runs $M=60$ elements were used. Bottom figure: the corresponding Hermite cubic collocation pressure gradients $K=1, 2, 4, 8, 16$, and 32. These results closely resemble those given in [32].

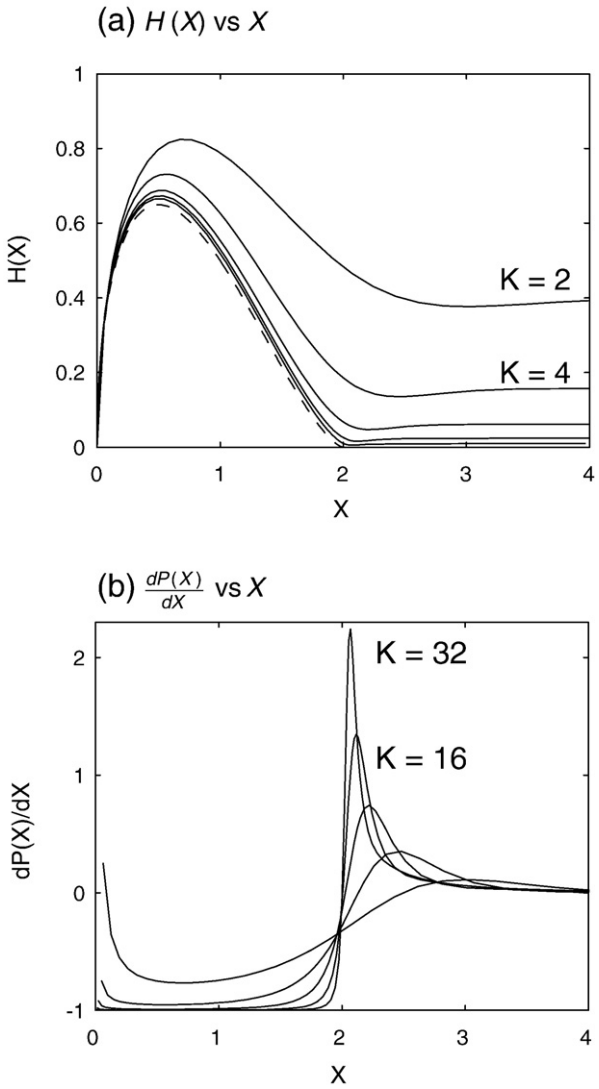

Fig. 8. Top figure: the scaled Hermite cubic collocation fracture half-widths $H(X)$ for $K=1, 2, 4, 8, 16$, and 32 are plotted with solid lines. The dashed line represents the analytic solution for the head $H_0 = \frac{1}{2}X^{1/2}(2-X)^{3/2}$. In all these runs $M=60$ elements were used. Bottom figure: the corresponding Hermite cubic collocation pressure gradients $\frac{dP}{dX}$ are also plotted for the same range of K values. These results closely resemble those given in [32].

introduced in Section 3 as well as the infinite element influence function H^{∞}, defined in Eq. (4.4), as follows:

$$C^0_{k2} = \lambda \mathcal{H}^e_-(x_k - x_2, \Delta_1, \Delta_2, \alpha)$$
$$C^0_{kl} = \lambda \mathcal{H}^0(x_k - x_l, \Delta_{l-1}, \Delta_l),\ l = 3:M$$
$$C^0_{kM+1} = \lambda \mathcal{H}^{\infty}(x_k - x_M, \Delta_M)$$

and

$$C^1_{kl} = \lambda \mathcal{H}^1(x_k - x_l, \Delta_{l-1}, \Delta_l),\ l = 3:M$$

here $\alpha = 1/2$ and, in accordance with the elasticity Eq. in (4.2), we define $\lambda = -\frac{1}{\pi}$.

In Fig. 7(a) we plot the Hermite cubic collocation fracture half-widths $h(x)$ for the following sequence of values for the fracture toughness $K = 1, 2, 4, 8, 16$, and 32. In all these runs $M = 60$ elements were used and crude mesh refinement was used in the vicinity of the left tip as well as near the anticipated minimum point in the half-width field, which corresponds to the neck that is adjacent to the bulbous fracture head. For large K the approximate location of this neck occurs at $x = 2K^{2/3}$.

The method used by [32] had difficulty resolving the peak in p' for values of $K \geq 16$ due to the mesh distribution. In order to explore the solution for values of $K \geq 16$, Roper and Lister introduced the scaling

$$X = \frac{x}{K^{2/3}},\ H = \frac{h}{K^{4/3}},\ P = \frac{p}{K^{2/3}},\ \frac{dP}{dX} = \frac{dp}{dx}$$

and formulated a new numerical scheme to solve the re-scaled equations.

In Fig. 8 we re-plot the same Hermite cubic collocation solutions as those presented in Fig. 7, but in the scaled coordinates. We observe that the method presented in this paper is able to faithfully reproduce these results without re-scaling.

5. Conclusions

In this paper we have presented a novel algorithm based on cubic Hermite interpolation to solve the coupled integro-partial differential equations governing a hydraulic fracture propagating in a state of a plane strain. The influence functions needed to implement the algorithm have been evaluated explicitly and are provided for completeness. Of particular importance for the analysis of hydraulic fractures, is the influence function associated with a blended cubic Hermite-power–law basis function, which is valid for any power–law index $0 < \alpha < 1$. In addition, the formulation is extended to treat semi-infinite domains by the incorporation of a blended cubic Hermite-constant element. Indeed, the infinite element influence function associated with an arbitrary power–law (only restricted by the constraint that the resulting improper integral should be convergent) can also be evaluated analytically in much the same way as for the blended tip elements.

In the numerical experiments presented, the cubic Hermite scheme was shown to converge to the similarity solution for a viscosity dominated plane strain HF propagating in an elastic medium with zero toughness. The convergence rate of the scheme for larger mesh sizes $O(\Delta\xi^{2.43})$ is dominated by the largest neglected term in the tip asymptotic expansion. However, as the mesh is refined further, the error decreases rapidly as the influence of the tip element becomes subdominant. Thus if an optimal order scheme is to be constructed the $O(h^4)$ accuracy within the domain needs to be matched by the order of the asymptotic expansion used to establish the tip solution. The backward Euler time-stepping scheme proved to be a robust and accurate time-stepping scheme for tracking the HF solutions tested. A simple scheme to increase the time-step geometrically between steps yields remarkably accurate results with little deterioration of the solution in spite of the large time steps used at the end of the simulation. This type of scheme will prove very useful when exploring the transition from one mode of propagation to another, which can take place over many orders of magnitude in the elapsed time. The cubic Hermite scheme performed equally well on the experiment to track the time dynamic solution of a plane strain HF propagating in the large toughness regime. The flexibility of the technique was also demonstrated by the application to the model of a steady, semi-infinite buoyancy driven HF propagating in a large toughness regime. The cubic Hermite results correlated well with the published solution and managed to achieve accurate results for relatively large dimensionless toughnesses without requiring a re-scaling of the problem.

A number of extensions and enhancements to the algorithm are possible. For example incorporating leak-off into this model using the 5/8 asymptote [4,22] is relatively straightforward given the fact that the expressions for the blended influence functions have been established for arbitrary $0 < \alpha < 1$. It is desirable to apply the method developed here to more complex problems in which rapid changes in the solution can be expected to occur spontaneously within the domain — such as the formation of pinch points in the vicinity of discontinuities in the ambient geological stress field σ_c. In this case it may be necessary to develop some form of adaptive mesh refinement in regions in which the gradients of the solution are large. Adaptive time-stepping might also be necessary to capture the time scale on which the pinch point forms. Because the plane strain Cauchy kernel (Eq. (2.2)) appears as the dominant, singular part to many fracture propagation models, the tools developed in this paper will also prove useful in the development of HF models for other fracture geometries such as radial fractures or slender fractures.

The method presented in this paper establishes a flexible framework for the analysis of plane strain hydraulic fractures. It yields accurate results when tested against established solutions to problems with different tip asymptotes. The arbitrary power–law blended tip elements and robust time-stepping open the possibility to explore the transition of asymptotes as the propagation regime changes from one regime to another, provided the tip element is sufficiently small that the correct power–law active at the tip can be used. To represent such a transition from one power–law to another on a coarser mesh, we could use an effective power–law that is chosen to match the same volume of fluid in the tip as that given by the detailed transition solution. Finally, the accurate solution with relatively modest computational resources provided by this algorithm also opens the possibility of deployment within algorithms to model planar fractures in 3D elastic media to provide autonomous tip asymptotic solutions that can model different propagation regimes at different points along the periphery of the planar fracture.

Acknowledgements

The author gratefully acknowledges the grant support of NSERC (Canada). In addition the author would like to thank Professor Emmanuel Detournay, from the University of Minnesota, for many useful discussions during the development of this project and Drs. J Adachi and D. Garagash for help in obtaining accurate comparison solutions.

Appendix A. Asymptotic behavior of Π

In this appendix we use a Mellin transform analysis (see [24]) to determine the tip asymptotic behavior of the pressure field Π for a finite crack associated with a width field Ω having a given power–law behavior in the neighborhood of one of the tips. By introducing a coordinate system located at one of the tips of the fracture, it is possible to rewrite Eq. (2.12) in the following form

$$\Pi(\xi) = -\frac{1}{4\pi\gamma} \Xint{=}_0^2 \frac{\Omega(\chi)}{(\chi - \xi)^2} d\chi. \tag{A.1}$$

We define the Mellin transform (see [24,29]) of $\Pi(\xi)$ to be

$$\hat{\Pi}(z) = \int_0^\infty \xi^{z-1}\Pi(\xi)d\xi.$$

If $\Pi(\xi)$ has the following asymptotic behaviors

$$\Pi(\xi)\sim\begin{cases}\xi^{\beta} \text{ as } \xi\to 0\\ \xi^{-\theta} \text{ as } \xi\to\infty\end{cases}$$

then $\hat{\Pi}(z)$ is analytic on the strip $-\beta<Re(z)<\theta$. The function Π may be recovered by the Bromwich type inversion integral

$$\Pi(\xi) = \frac{1}{2\pi i}\int_{c-i\infty}^{c+i\infty} \xi^{-z}\hat{\Pi}(z)dz \tag{A.2}$$

in which c lies in the above strip of analyticity. By considering the limiting behavior of $\Pi(\xi)$ as $\xi\to\infty$ in (A.1), we conclude that $\Pi(\xi)\sim\xi^{-2}$ so that $\theta=2$.

Now applying the integral operator $\int_0^\infty \xi^z d\xi\bullet$ to (A.1) we obtain

$$-\frac{1}{4\pi\gamma}\int_0^\infty \xi^z\left(\int_0^2 \frac{\Omega(\chi)}{(\chi-\xi)^2}d\chi\right)d\xi = \hat{\Pi}(z+1).$$

Assuming that we may swap the order of integration, and using the following Mellin transform [24]

$$\int_0^\infty \frac{\xi^z}{(\chi-\xi)^2}d\xi = -\pi z\chi^{z-1}\cot\pi z, \text{ which is analytic for } -1<Re(z)<1,$$

we obtain the following equation

$$\frac{z\cot\pi z}{4\gamma}\int_0^2 \Omega(\chi)\chi^{z-1}d\xi = \hat{\Pi}(z+1). \tag{A.3}$$

By defining $\Omega(\xi)=0$ for $\xi>2$, and using the fact that Ω vanishes at $\xi=2$ we may define a continuous extension of Ω to the whole interval $[0,\infty)$. Using this extension we may rewrite (A.3) as follows

$$\frac{z\cot\pi z}{4\gamma}\hat{\Omega}(z) = \hat{\Pi}(z+1), \tag{A.4}$$

which, in view of the region of analyticity of Π, must be analytic in the strip

$$-\beta-1<Re(z)<1.$$

Now assuming the following asymptotic behavior for Ω

$$\Omega(\xi)\sim A\xi^{\alpha} \quad 0<\alpha\le 1$$

it follows that $\hat{\Omega}(z)$ has a simple pole at $z=-\alpha$ of the form

$$\frac{A}{z+\alpha}.$$

Moreover, given that Ω vanishes for $\xi\ge 2$ it follows that $\hat{\Omega}(z)$ is analytic in the half-space $-\alpha<Re(z)$. In order for the regions of analyticity of $\hat{\Omega}(z)$ and $\hat{\Pi}(z+1)$ to match for $\alpha<1$, we require that $-\beta-1=-\alpha$, since the $z\cot\pi z$ factor (A.4) in does not interfere with the region of analyticity, except if $\alpha=1$. Now in order to obtain the asymptotic behavior of Π we push the contour in (A.2) downhill (to the left to obtain the asymptotic behavior as $\xi\to 0$) until we encounter the first pole. The leading behavior is obtained from the residue at that pole, which can be shown to yield

$$\Pi(\xi)\sim\begin{cases}\frac{A}{4\gamma}\alpha\cot\pi\alpha\,\xi^{\alpha-1} \text{ for } 0<\alpha<1\\ \frac{A}{4\pi\gamma}\log\xi \text{ for } \alpha=1\end{cases}$$

Note that in the special case $\alpha=1/2$ the pole is removed by the $\cos\pi z$ term in the numerator of the pre-factor multiplying $\hat{\Omega}(z)$ in (A.4). In addition, the log term results from the double pole due to the $\sin\pi z$ term in the denominator of same pre-factor as $z\to -1$.

References

[1] M. Abramowitz, I. Stegun, Handbook of Mathematical Functions with Formulas, Graphs, and Mathematical Tables, Dover Publications Inc., New York, 1972.
[2] A.S. Abou-Sayed, D.E. Andrews, I.M. Buhidma, Evaluation of oily waste injection below the permafrost in Prudhoe Bayfeld, Proceedings of the California Regional Meetings, Bakersfeld, CA, Society of Petroleum Engineers, Richardson, TX, 1989, pp. 129–142.
[3] Abou-Sayed, A.S., Safe injection pressures for disposing of liquid wastes: a case study for deep well injection (SPE/ISRM-28236), in: Balkema (Ed.), Proceedings of the Second SPE/ISRM Rock Mechanics in Petroleum Engineering, 769–776, 1994
[4] Adachi, J.I., Fluid-Driven Fracture in Permeable Rock, Ph.D. Thesis, University of Minnesota, 2001; available at www.umi.com.
[5] J.I. Adachi, E. Detournay, Self-similar solution of a plane-strain fracture driven by a power–law fluid, Int. J. Numer. Anal. Meth. Geomech. 26 (2002) 579–604.
[6] J.I. Adachi, E. Detournay, Plane-strain propagation of a fluid-driven fracture in a permeable medium, Engrg. Fract. Mech. 75 (2008) 4666–4694.
[7] U.M. Ascher, R.M.M. Mattheij, R.D. Russell, Numerical solution of boundary value problems for ordinary differential equations, volume 13 of Classics in Applied Mathematics, Society for Industrial and Applied Mathematics (SIAM), 1995.
[8] G.K. Batchelor, An Introduction to Fluid Dynamics, Cambridge University Press, Cambridge, U.K., 1967
[9] R. Carbonell, J. Desroches, E. Detournay, A comparison between a semi-analytical and a numerical solution of a two-dimensional hydraulic fracture, Int. J. Solids Struct. 36 (1999) 4869–4888.
[10] M. Cleary, S. Wong, Numerical simulation of unsteady fluid flow and propagation of a circular hydraulic fracture, Int. J. Numer. Anal. Meth. Geomech. 9 (1985) 1–14.
[11] C. De Boor, A Practical Guide to Splines, Springer-Verlag, New York, 1978.
[12] J. Desroches, E. Detournay, B. Lenoach, P. Papanastasiou, J.R.A. Pearson, M. Thiercelin, A.H.D. Cheng, The crack tip region in hydraulic fracturing, Proc. R. Soc. London, Ser.A vol. 447 (1994) 39–48.
[13] E. Detournay, Propagation regimes of fluid-driven fractures in impermeable rocks, Int. J. Geomech. 4 (1) (2004) 1–11.
[14] E. Detournay, A.H.D. Cheng, J.D. McLennan, A poroelastic PKN hydraulic fracture model based on an explicit moving mesh algorithm, ASME J. Energy Resour. Technol. 112 (1990) 224–230.
[15] M.J. Economides, K.G. Nolte (Eds.), Reservoir Stimulation, John Wiley & Sons, Ltd., New York, 2000.
[16] R.G. Jeffrey, K.W. Mills, Hydraulic fracturing applied to inducing longwall coal mine goaf falls, Pacific Rocks 2000, Balkema, Rotterdam, 2000, pp. 423–430.
[17] D.I. Garagash, E. Detournay, Plane-strain propagation of a fluid-driven fracture: small toughness solution, ASME J. Appl. Mech. 72 (6) (2005) 916–928.
[18] D.I. Garagash, Plane-strain propagation of a fluid-driven fracture during injection and shut-in: asymptotics of large toughness, Eng. Fract. Mech. 73 (2006) 456–481.
[19] L.J. Gray, M. Garzon, On a Hermite boundary integral approximation, Comput. Struct. 83 (2005) 889–894.
[20] D.A. Hills, P.A. Kelly, D.N. Dai, A.M. Korsunsky, Solution of crack problems, The Distributed Dislocation Technique, Solid Mechanics andits Applications, vol. 44, Kluwer Academic Publisher, Dordrecht, 1996.
[21] J.A. Kierzenkaand, L.F. Shampine, A BVP solver based on residual control and the MATLAB PSE, ACM Trans. Math. Softw. 27 (3) (2001) 299–316.
[22] B. Lenoach, The crack tip solution for hydraulic fracturing in a permeable solid, J. Mech. Phys. Solids 43 (1995) 1025–1043.
[23] J.R. Lister, Buoyancy-driven fluid fracture: the effects of material toughness and of low-viscosity precursors, J. Fluid Mech. 210 (1990) 263–280.
[24] P.A. Martin, End-point behaviour of solutions to hypersingular integral equations, Proc. Roy. Soc. London 432 (1991) 301–320.
[25] S.L. Mitchell, R. Kuske, A.P. Peirce, An asymptotic framework for the analysis of hydraulic fractures: the impermeable case, ASME J. Appl. Mech. 74 (2) (2007) 365–372.
[26] K.H. Muci-Kuchler, T.J. Rudolphi, Coincident collocation of displacement and tangent derivative boundary integral equations in elasticity, Int. J. Numer. Meth. Eng. 36 (1993) 2837–2849.
[27] K.H. Muci-Kuchler, T.J. Rudolphi, Application of tangent derivative boundary integral equations to the formulation of higher order boundary elements, Int. J. Solids Struct. (1994) 1565–1584.
[28] K.H. Muci-Kuchler, J.C. Miranda-Valenzuela, A new error indicator based on stresses for adaptive meshing with Hermite boundary elements, Eng. Anal. Bound. Elem. 23 (1999) 57–670.

[29] F. Oberhettinger, Tables of Mellin Transforms, Springer-Verlag, NY, 1970.
[30] A. Peirce, E. Detournay, An implicit level set method for modeling hydraulically driven fractures, Comput. Meth. Appl. Mech. Eng. 197 (2008) 2858–2885.
[31] J.R. Rice, in: H. Liebowitz (Ed.), Mathematical Analysis in the Mechanics of Fracture, Fracture, an Advanced Treatise, Academic Press, New York, 1968, pp. 191–311, Chap. 3.
[32] S.M. Roper, J.R. Lister, Buoyancy-driven crack propagation: the limit of large fracture toughness, J. Fluid Mech. 580 (2007) 359–380.
[33] D.A. Spence, P. Sharp, Self-similar solutions for elastohydro dynamic cavity flow, Proc. R. Soc. London, Ser. A 400 (1985) 289–313.
[34] D.A. Spence, P.W. Sharp, D.L. Turcotte, Buoyancy-driven crack propagation: a mechanism for magma migration, J. Fluid Mech. 174 (1987) 135–153.
[35] A. van As, R.G. Jeffrey, Caving induced by hydraulic fracturing at North Parkes mines, Pacific Rocks 2000, Balkema, Rotterdam, 2000, pp. 353–360.
[36] J.O. Watson, Hermitian cubic and singular elements for plain strain, in: P.K. Banerjee, J.O. Watson (Eds.), Developments in Boundary Element Methods, vol. 4, Elsevier Applied Science Publishers, London and New York, 1986, pp. 1–28, Chapter 1.